Julius-Maximilians-Universitaet Wuerzburg
Fakultaet fuer Physik und Astronomie
Lehrstuhl fuer Astronomie

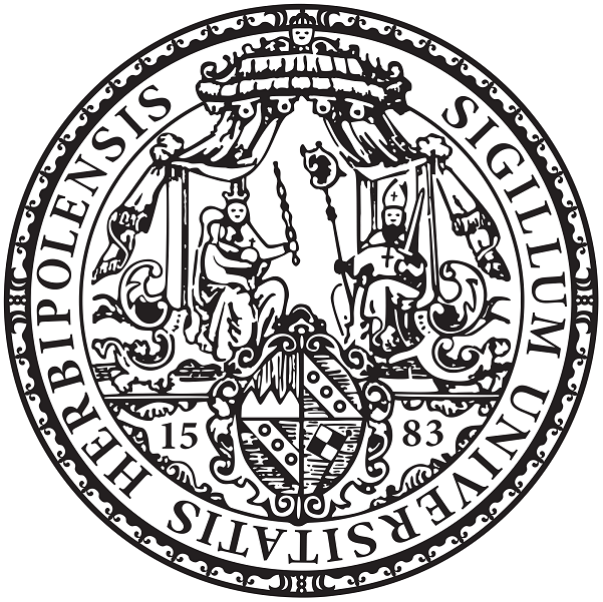

Bachelor Thesis

VLBI Observations of the Flat-Spectrum-Radio-Quasar PKS 1454-354

Author: Stefan Lindeholz
Supervisor: Prof. Dr. Matthias Kadler
Date of Submission: February 15, 2017

Zusammenfassung

In dieser Arbeit werden Aktive Galaxienkerne mittels Radio Interferometrie untersucht. Aktive Galaxienkerne sind dabei sehr helle Quellen am Himmel, die über das gesamte elektromagnetische Spektrum Strahlung emittieren. Das Spektrum ist dabei durch zwei Strahlungsprozesse dominiert, nämlich der Synchrotron Strahlung und der inversen Comptonstreuung. Aktive Galaxienkerne weisen teilweise sehr unterschiedliche Charakteristika auf, die sich allerdings durch das Vereinheitlichungsmodell auf mit einem einheitlichen Schema erklären lassen. Diese Aktiven Galaxienkerne weisen häufig Kegel auf, die eine hohe Radioemission besitzen. Diese werden häufig als Jets bezeichnet und hinsichtlich ihrer Bewegung untersucht, da sich daraus viele Daten über den Galaxienkern treffen lassen. Die Knoten in den Jets breiten sich teilweise mit Geschwindigkeiten aus, die jenseits der Lichtgeschwindigkeit liegen, was durch Projektionseffekte erklärt werden kann.
Um die Aktiven Galaxienkerne und vielmehr ihre Jets im Radiobereich untersuchen zu können, ist es nötig hohe Auflösungen zu erzielen um die inneren Strukturen sehen zu können. Dies ist durch die hohe Wellenlänge im Radiobereich erschwert, was sehr große Teleskope notwendig macht. Um die Teleskope künstlich zu vergrößern werden mehrere Teleskope mithilfe der Very Long Baseline Interferomtry zu Arrays zusammengeschlossen. Die Größe dieses Teleskops entspricht dann der Basislinie zwischen den am weitesten auseinander stehenden Teleskopen. Das TANAMI Programm realisiert ein solches Array um in der südlichen Hemisphäre die Aktiven Galaxienkerne zu untersuchen. Um diese Daten auszuwerten sind spezielle Algorithmen notwendig, da diese Arrays nur die Fourier-Transformation, des zu untersuchenden Objekts sehen. Durch numerische Verfahren wird dies zurück transformiert um eine Radiokarte des Objekts zu erhalten.
An dem Beispiel des Aktiven Galaxienkerns PKS 1454-354 werden diese Verfahren angewendet. Dabei wurden sieben verschieden Zeitepochen untersucht, die während eines Gammastrahlen Flares aufgezeichnet wurden. Flares beschreiben Zustände wo sich die Flussdichte, über kurze Zeiträume, um einen signifikanten Wert erhöht. Zur Untersuchung wurden zuerst die Fluss-bereinigten Radiokarten erstellt und anschließend die Komponenten im Jet modelliert. Mithilfe der Berechnung der linearen Regression über den Radius konnte die scheinbare Geschwindigkeit berechnet werden. Diese beläuft sich auf das $v = (-51 \pm 42)$-fache der Lichtgeschwindigkeit. Außerdem konnte ein Limit für den Winkel zur Sichtlinie auf $\varphi < 44°$ abgeschätzt werden.
Die gemessenen Flussidichten im Radiobereich konnten mit Daten aus anderen Wellenlängen verglichen werden um so den Versatz zwischen den zeitverschiedenen Flare-

Maxima festzustellen.

Abstract

In this thesis, Active Galactic Nuclei are researched, using radio interferometry. Active Galactic Nuclei are bright sources at the sky, which emitts electromagnetic radiation over the whole spectrum. Those radiation is mainly produced through two main radiation processes. The first one is the synchrotron radiation, the second one is through inverse compton scattering. Active galactic nuclei show some different properties, which can be explained through the unification modell. This states the charakteristic is mostly dependent on the angle under we look at the nucleus. Active galactic nuclei emitt often relativistic plasma along a conical lobe, which is called jet. Those show strong radio emission, which we can use to gain a lot of information about the jet. The components of the jet are moving often with velocitys above the speed of light. This can be explained by a projecton effect called super luminal motion.
Our main goal is to analyse the data in the radio regime and therefore we need to observe the regions near the core. Radio observations often have problems in the resolution, due to the high wavelengths. The resolution is limited by the size of the telescope, which has it maximum to constructional constraints. One solution is to use several telescopes together in an array and thus building a large telescope, since the resolution is the limited by the length of the baselines between the telescope. This technique is called VLBI. The TANAMI program is such a collaboration of telescopes in the southern hemisphere, which observes active galactic nuclei at 8.4 GHz. The technique of VLBI is using some special algorithms, sincee the measured signal is the fourier transformed image. Therefore numerical solutions are needed to gain the clean images out of the data.
In this work the active galactic nucleus PKS 1454-354 is observed at seven different time periods. During the observation period a flaring state was measured, a significant rise in the flux density of the source. The seven time epochs were imaged in the clean files and the components of the jet were modelfitted to calculate the velocity. A linear regression over the distance to the core leads to $v = 51 \pm 42$ times the speed of light. Also the angle to the line of site could be estimated to be lower than $\varphi = 44°$.
Also the observed radio flux densitys could be compared to the flux density of other wavelength measuring a difference of the time where the flux reaches its maximum.

Contents

1 Motivation

In the 20th century it was discovered, that amongst sources which was listed as stars, there were many with a way to high redshift. Further research on these objects revealed that they only look like stars in the optical regime but emitt radiation over the whole electromagnetic spectrum. These quasi-stellar sources, which hence was named Quasars, were the first objects, of a new kind of researched celestial objects. All of them had in common, that they were positioned in the middle of the resembling galaxy thus leading to the categorization as active galactic nuclei. With expanding the observed spectrum to radio, X-ray and γ radiation, there were more objects, which fitted the characteristic of centering the galaxy.
Currently the research of active galactic nuclei is one of the most interesting part of todays astrophysics. The emission of the galactic nulei is powered by mass accretion of black holes leading to very high luminosities. This enables us to see them at very high cosmological redshifts. Thus observing these objects reveals more information about earlier stages of the universe. Another reason why they are interesting is, because many of the active galactic nuclei emitt conical plasma jets. The observation of those, yields many new information about plasma physic and magnetohydrodynamics on larger scales and the processes which lead to this emission.
Some of the active galactic nuclei show very high variability on short time scales an example is the flat-spectrum- radio-quasar PKS 1454-354. This source was observed in the radio regime and during the observation a γ-ray survey discovered very high flux variations. There was plenty of followed up observations in all kinds of wavelength making this an excellent candidate to analyse. In the following thesis, the physics of active galactic nuclei will be discussed and the radio data during the flare and after it will be analysed.

2 Theoretical Background

2.1 Active Galactic Nuclei

Active Galactic Nuclei (AGN) are compact luminous regions in the center of galaxies. Because the origin of the luminosity is not caused by black body radiation as in stars, the luminosity of the AGN overwhelms by far the light of the respective galaxy. Every AGN is centered by a Super-Massive Black Hole (SMBH) producing the energy. The SMBH is surrounded by an accretion disc, which supplies mass, to convert it into energy through binding of the gravitaional energy. The most interesting part of the AGN are the so called jets, which are cones perpendicular to the torus. These contain highly relaivistic material which can be observed in the radio regime of the electromagnetic spectrum. AGN radiate over the whole spectrum which is due to two major radiation processes. The first one is Bremsstrahlung also known as synchrotron radiation, the second one is the inverse Compton scattering. These results in the characteristical Spectral Energy Distribution (SED) with double hump structure. These can roughly be fitted with a power law. The following section shows a short overview on the properties of AGN such as different classification, radiation processes and beaming effects, and is, if not highlighted otherwise, based on the textbook by Kembhavi et al. (13).

2.1.1 Classification of Different AGN

There are some approaches to sort AGN into different categories. A prposed by Kellermann et al. (12), the AGN can be differentiated based on their radio flux. This can be done by comparing the integrated radio flux to the one in the optical regime, resulting in the following equation

$$R_{r-o} = \frac{S_r}{S_o}. \tag{2.1.1}$$

Based on this the AGN counts as radio-quiet if $0.1 < R_{r-o} < 1$, otherwhise it is radio-loud if the resulting quotient is $R_{r-o} > 10$. BAsed on this categorization one can find that 10% of the AGN are radio-loud.

To further improve the categorization the spectrum can be taken into account. This results in the following list of properties in AGN spectra.

Seyfert Galaxies

Seyfert Galaxies are usually found in spiral galaxies. As Quasars they are defined by being star like, but there are some distinctions between them. Seyfert Galaxies are radio quiet galaxies and show a lower luminosity than Quasars. In addition they show characteristic broad and narrow emission lines. According to those emission lines we can further split the Seyfert galaxies into two groups.

Galaxies of the Seyfert Type I have continuous emission in the regimes of the X-ray and infrared, and develop broad emission lines as well as narrow ones. Galaxies of the Seyfert Type II show a very weak continuum but produce strong narrow emission lines.

Quasars

Quasars are based historically on the 'quasi-stellar-objects' (QSO) which are defined as star-like looking objects. The main distinction between QSO and Quasars is that Quasars produce a high radio signal. Usually Quasars are found at high redshifts and are limited to redshifts smaller than $z < 0.1$. To avoid confusing low flux Quasars with Seyfert Galaxis a differentiation of magnitude in flux is added.

Radio Galaxies

Radio galaxies have the main characteristic of an elliptical host galaxy. They produce strong continuos radiation in the optical regime. They can be classified like Seyfert galaxies using their spectral emission lines. The Broad Line Radio Galaxies (BLRG) have broad emission lines like Seyfert I, but in the radio regime. Similarly the Narrow Line Radio Galaxies (NLRG) show narrow emission lines like the Seyfert II. Radio galaxies show very high flux densitys in the radio regime and are also called radio loud. Another differentiation can be made observing the radio aspects of the galaxies. This was proposed by Fanaroff and Riley (1974). FR I galaxies are bright sources which can only be observed on large scales. The two jets are not visible near the core and build cloud shaped structures on the outer part of the galaxie. FR II are defined through lobed jets, which end in hotspots with high flux values. In FR II galaxies the counterjet is very weak in comparison to the main jet and can sometimes not be visible.

Blazars

The group of Blazars consists out of BL Lacertae (BL Lac) objects and 'Flat Spectrum Radio Quasars' (FSRQ). They mainly consists of a very strong continuous spectrum which heavily outweighs the thermal radiation mechanisms. They belong to the objects with the highest luminosity. This assumes to have its origin in relativistic beaming effects. Blazars show very high variability on short time scales.

The subclassification of the BL Lac objects has the characteristic of very weak emission lines, unlike the FSRQs which can show emission lines. BL Lac can usually be attributed

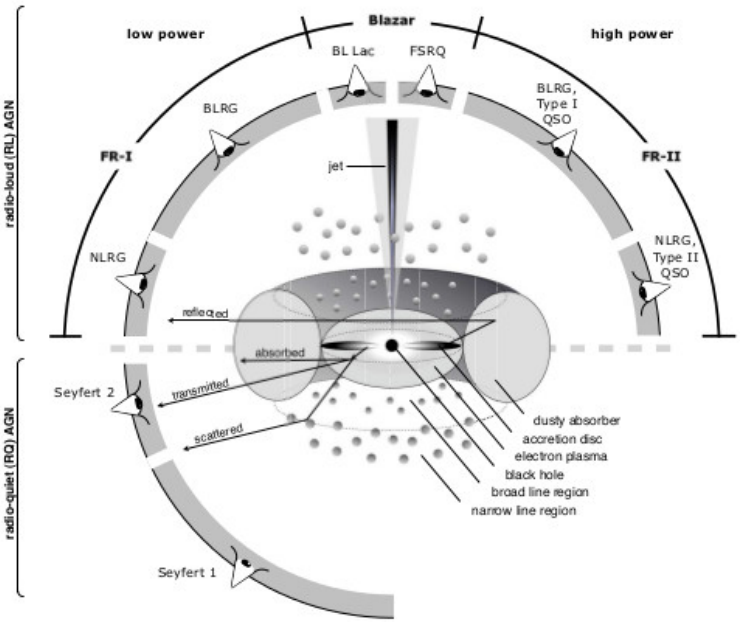

Figure 2.1: Scheme of the different viewing angles on the AGN, the upper half resembles the radio-loud AGN, where if we look edge-on the broad line region of the jet is covered by the dusk torus, thus we see is only the NLR. Increasing the angle makes the BLR visible, and we see a BLRG. At highest angles we look directly in the jet and we see the very luminous quasars. The image is taken from Beckmann et al. (3).

to X-ray sources as well.

2.1.2 Unification Model

Antonucci (2) and Urry et al. (21) proposed that any given AGN Type is based on the same structure, but which type we see is only dependent on which angle we are looking at it. The scheme in Fig. 2.1 illustrates that. The basic model assumes a SMBH in the center of the AGN. This is surrounded by a hot accretion disc, which provides the mass for the gravitational energy. An optical opaque torus out of cold dust encloses the inner core. The other important regions for the optical regime are the broad line region (BLR) and the narrow line region (NLR) which are hosting processes, causing the emission lines in the spectrum. The physical properties of the resembling regions can be found in Table 2.1.

With this further knowledge we can sort the different viewing angles to the different properties of the model. Starting with Seyfert I galaxies we look directly into the black hole in a radio-quiet AGN thus seeing the BLR and the NLR and thus having both emission characteristics in the spectrum. Decreasing the viewing angle results in blocking the view on the BLR and leaving only the narrow lines in the spectrum to see.

Region	Radius R in pc	Density n in cm^{-3}	velocity v
Accretion disc	10^{-3}	10^{15}	$0.3c$
Dust torus	$1 - 10$	$10^{3} - 10^{6}$	-
BLR	$0.01 - 0.1$	10^{10}	$1000 - 5000\text{kms}^{-1}$
NLR	$100 - 1000$	$10^{3} - 10^{6}$	few 100kms^{-1}

Table 2.1: Parameters in the different jet regions, shown in the table are the extensions of the regions, the density of the particals and the medium velocity of those. The data of the table is taken from the lecture of Kadler (10)

Type	Optical lines	Radio-quiet	Radio-loud
Type I	Broad and narrow lines	Seyfert I	BLRG/FSRQs
Type II	Narrow lines only	Seyfert II	NLRG
Type 0	No lines	-	BL Lac

Table 2.2: Overview over the AGN-zoo, adapted from Beckmann et al. (3)

If we look on a radio loud galaxy an additional component is the jet lobe. Starting with the NLRG we see only the NLR because the viewing angle does not allow to see the BLR due to of the dust torus. If we increase the viewing angle the BLR becomes visible again like we see it in the BLRG. At the highest angles around 90° we almost look directly into the jet. Because of the relativistic properties of the jet we get beaming effects, which will be explained further later, resulting in a very luminous Blazar. For Comparison with Fig. 2.1 the properties of the different morphologies can be found in Table 2.2.

2.1.3 Radiation Processes in AGN

Since there is a large area of the electromagnetic spectrum covered, an important question one has to ask is how the radiation is produced. If looking at an SED of an AGN, the so called double hump structure can always be seen. This phrase comes from two power law fits which, in logarithmic scaling, becomes parabola shaped. This indicates that we have to discuss two major processes which are causing this characteristic form. The following section is based on the textbook by Beckmann and Shrader (3).

Synchrotron Radiation

If charged particles are accelerated in a magnetic field one has to take the Lorentz force into equation, which is given by

$$\frac{d}{dt}(\gamma m\vec{v}) = \frac{Ze}{c}(\vec{v} \times \vec{B}), \tag{2.1.2}$$

where γ resembles the Lorentzfactor $\gamma = (\sqrt{1 - \frac{v^2}{c^2}})^{-1}$, m the mass of the particle, v the velocity, Z the amount of charges in the particle, c the speed of light and $\vec{B}$ the magnetic field strength. We can split the acceleration into a longitudinal and an transversal aspect. If we look at the acceleration along the magnetic field line, one can easy see that the Lorentz force equals zero so nothing will be changed at longitudinal velocity. If we look at acceleration transversal to the field line the velocity is perpendicular to the magnetic field resulting in a change of velocity. This leads to a helicular motion around the magnetic field line, where the gyration frequency is given by

$$\nu_g = \frac{ZeB}{2\pi\gamma mc}. \tag{2.1.3}$$

Taking into account that the longitudinal velocity is equal to zero we can express the velocity as a function of the pitch angle β. This leads to the luminosity L, according to Rybicki and Lightman (19)

$$L = \frac{2Z^4e^4B^2\gamma^2v^2\sin^2\beta}{3c^5m^2} \tag{2.1.4}$$

Since the radiation will not be emitted isotropically, but in a cone like shape, we can assume $\Phi \simeq \gamma^{-1}$ for the opening angle resulting in a lighthouse effect. So the result is a pulsed emission where the gyration period is much wider than the pulse width. Using this relation calculates with some further steps and by inserting the critical velocity the luminosity of our cone, which is given by

$$L(E, v) = \frac{\sqrt{3}Z^3e^3B\sin\beta}{mc^2} \cdot F(x). \tag{2.1.5}$$

With the relation $x = \frac{\nu}{\nu_c}$, where ν_c is the critical frequency, this leads to

$$F(x) = \frac{\nu}{\nu_c}\int_{v/v_c}^{\infty} K_{5/3}(\xi)d\xi. \tag{2.1.6}$$

In this case $K_{5/3}$ resembles the modified Bessel function of the order 5/3. This leads to the spectrum for the lower energies.

Inverse Compton Scattering

Compton scattering describes a photon with high energy, which is refracted at an electron and thus resulting in accelerating the electron. For inverse Compton scattering the opposite is the case. We have highly relativistic matter in our jet. This leads to an electron transferring energy to a photon and lifting it to very high energies. We can use the Doppler shift formula to calculate the energy of the photon with:

$$h\nu' = \gamma h\nu(1 + \frac{\nu_e}{c}\cos\theta), \tag{2.1.7}$$

where ν and ν' describes the energies of the photon before and after the collision, ν_e the energy of the electron and θ the collision angle. The source of the electrons for the inverse Compton scattering is provided by the jet itself through the synchrotron radiation. This effect is called synchrotron self Compton (SSC). While the luminosity of the synchrotron radiation is proportional to the magnetic field density U_B, the SSC luminosity depends on the energy density of the photon field U_{rad}, thus leading to

$$\frac{L_{\mathrm{SSC}}}{L_{\mathrm{sync}}} = \frac{U_{\mathrm{rad}}}{U_{\mathrm{B}}}. \tag{2.1.8}$$

Since these processes are highly correlated to each other and the up-scattered photons influence the photon field, there will be a point in brightness temperature where the system collapses. This so called Compton catastrophe happens if the brightness temperature exceeds one critical point ($10^{12}K$), when the electrons are getting cooled very efficiently. So in this source SSC radiation will be dominant.

2.1.4 Brightness Temperature

Since it was already mentioned above, we have to sort out the term of brightness temperature. This is a very important quantity if dealing with AGN astronomy and especially in the radio regime. If we are modelfitting jet components, it is the best option to use Gaussian components of a given flux density until the model resembles the data. These components are oftenly described with a temperature a black-body would emitt to get the same frequency ν. According to Kovalev et al. (14) the brightness temperature is given by

$$T_b = \frac{2ln2}{\pi k}\frac{S_{\mathrm{core/component}}\lambda^2(1+z)}{\theta_{\mathrm{maj}},\theta_{\mathrm{min}}} \tag{2.1.9}$$

where λ is the wavelength, θ_{maj} and θ_{min} are the axes of the Gaussian components, z is the cosmological redshift of the source, k is the Boltzmann factor and $S_{\mathrm{core/component}}$ is the flux density of the core/component.

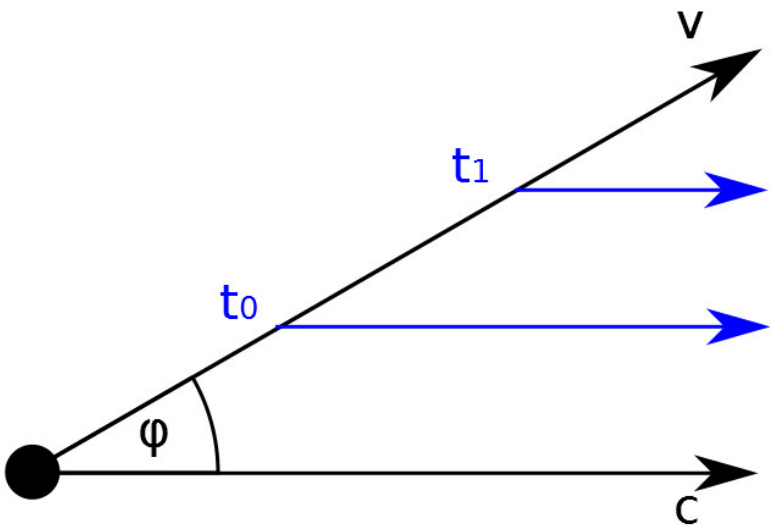

Figure 2.2: Scheme of the superluminal motion. The signals are emitted at different times thus resulting in a Doppler boosting. The image was created after the lecture of Kadler (10)

2.1.5 Jet Kinematic and Morphology

Most of the observed jets show components in the jet, that have velocities higher than the speed of light. This seems to contradict the theory of relativity completly on the first glance, but in the end it can be explained with a simple projection effect. Figure 2.2 scetches this.

Consider a jet which travels with a relativistic velocity v. The signal emittet at a given time t_0 travels with the speed of light c, thus reaching the observer at t_0'. When the time progresses to a further time $t_1 = t_0 + \Delta t$, the jet will have reached the distance $\Delta x = v \cdot \Delta t$. We can calculate the angle under which we see the movement to the relation:

$$\beta = \frac{v \Delta t \sin \varphi}{r}, \tag{2.1.10}$$

where r stands for the distance the jet had at the time t_2 and φ is the angle to the line of sight (LOS). If we calculate the time difference between the two points we get the equation

$$\Delta t' = \Delta t (1 - \frac{v}{c} \cos \varphi). \tag{2.1.11}$$

If we compare the apparent velocity perpendicular to the observer v_{app} to the speed

of light c we get following equation

$$\frac{v_{app}}{c} = \frac{v \sin \varphi}{c(1 - \frac{v}{c} \cos \varphi)}. \tag{2.1.12}$$

We can use Equation (2.1.12) to gain a formula to directly express the Lorentz factor $\beta = \frac{v}{c}$

$$\beta = \frac{\beta_{\text{app}}}{\beta_{\text{app}} \cos \varphi + \sin \varphi}. \tag{2.1.13}$$

Furthermore there is another important relativistic effect regarding the luminosity. Since the matter is getting closer to us there is a Doppler boosting effect. If we apply the formula for Doppler boosting on our blazar we get following equation:

$$D = \frac{\sqrt{1 - (\frac{v}{c})^2}}{1 - \beta \cos \varphi}. \tag{2.1.14}$$

Rybicki and Lightman (19) showed also that we get for the flux density S_ν

$$S(\nu_{\text{obs}}) = D^{3-\alpha} S(\nu_{\text{em}}). \tag{2.1.15}$$

if we insert a power law spectrum $S(\nu) = A\nu^\alpha$. With this knowledge we can also explain why we only see one-sided jets in blazars. If the Doppler boosting becomes strong through low angles, the sensitivity is not enough to see the counter-jet. In fact we can use this to estimate the Doppler factor and therefore estimate the jet to counter-jet ratio.

$$R = \frac{S_{\text{jet}}}{S_{\text{counterjet}}} = \left(\frac{1 + \frac{v}{c} \sin \varphi}{1 - \frac{v}{c} \sin \varphi} \right)^{i-\alpha} \tag{2.1.16}$$

2.2 Very Long Baseline Interferometry

Our main goal is to observe radio morphologies inside the AGN jets. Here occurs one big problem, which seems quite difficult on first sight. Usually the objects we are observing are far away. The angular resolution Θ can be calculated with the Rayleigh criteria to be

$$\Theta \approx 1,22 \frac{\lambda}{D}, \tag{2.2.1}$$

where λ is the observed wavelength and D the diameter of our telescope. We fill in for example a typical radio frequency of 1.4GHz, thus $\lambda = 21\,\text{cm}$, which is a famous spectral line of hydrogen in the radio regime. Adding the diameter of the biggest steerable radio telescope, which is the Green Bank telescope in Virginia(USA), with its $D = 101\text{m}$, we

get for the angular resolution $\Theta = 2.54 \cdot 10^{-3}$rad. This is by far not enough to resolve the jet structures we are looking at, so we need a more advanced strategy. This leads to the Very Long Baseline Interferometry (VLBI) which uses the baseline between a couple of radio dishes to create one large big virtual telescope and thus improving the resolution by far.

2.2.1 Theory of Radio Interferometry

We start with a single radio telescope. Because the flux which is received by the antenna is highly dependant on the observing wavelength, we can not rely on flux values. Therefore in radio astronomy we have to use the flux density S_ν which is defined as a given flux S in a wavelength regime $d\lambda$. The information of this section is taken from Burke and Graham-Smith (4) if not mentioned otherwise.

$$S = \int S_\nu d\nu, \tag{2.2.2}$$

where ν is the frequency of the input signal. If we want to calculate the total power the telescope is receiving we have to take the effective area A_{eff} of the telescope into account. Thus we can claculate the power to be

$$P = \int A_{\text{eff}} S_\nu d\nu. \tag{2.2.3}$$

The simplest VLBI instrument consists of two dishes, hence it is called two-element interferometer. A scheme of this interferometer can be seen in Fig. 2.3 on the left panel. There are some important parameters which define our telescopes, first the baseline b which is the distance between the two elements, and second the measured flux density on both dishes. We can use the baseline to calculate the phase difference, caused by the different light run time, to be $\tau_g = \vec{b} \cdot \vec{s}/c$. This is used in an amplifier to synchronize the two signals to the same phase, which can be used to calculate the cross-correlation product. The cross-correlation product is simply the two signals folded together $R_{xy}(\tau) \equiv \langle x(t)y(t-\tau)\rangle$. If we calculate the cross correlation for a monochromatic source and using the signals $x(t) = v_1 \cos(2\pi\nu t)$ and $y(t) = v_2 \cos[2\pi\nu(t-\tau_g)]$, we get

$$R_{xy}(\tau_g) = A(\vec{s}) S \cos(2\pi\nu\tau_g) = A(\vec{s}) S \cos(2\pi\nu \vec{b_\lambda} \cdot \vec{s}/c). \tag{2.2.4}$$

In this formula $\vec{b}$ has been expressed through $\vec{b_\lambda} = \vec{b}/\lambda$. In the part above, the time delay was set to zero so $\tau_i = 0$. Since this is not often the case we have to ease this restriction by setting $\tau_g = \tau_i$ as shown in Fig.2.3 on the right panel. The reference point is called the phase tracking center and will be expressed with $\vec{s}_0$. As shown in the scheme

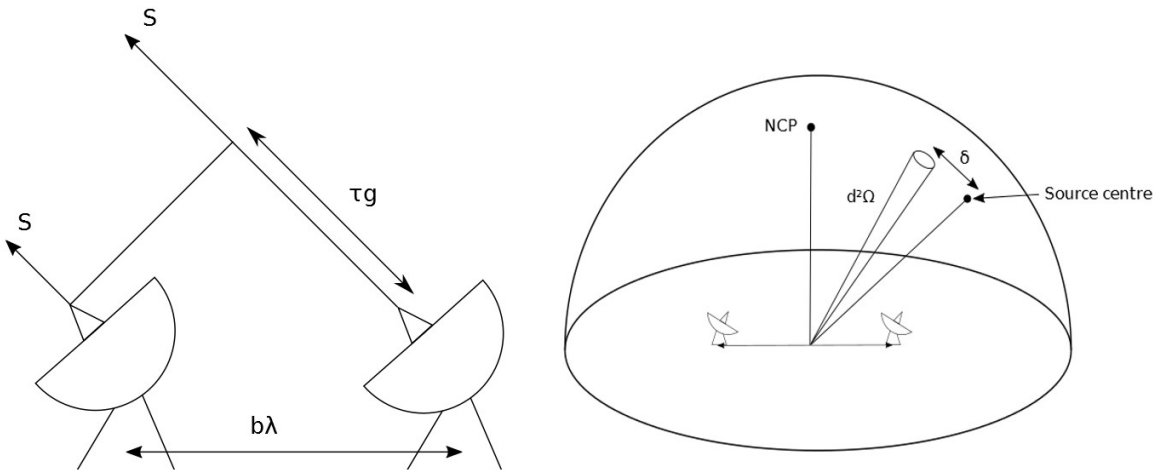

Figure 2.3: Left panel: Scheme of a two-element interferometer. The two dishes receive a signal S from the same source with a timedelay τ_g and are separated through the baseline b_λ. Right panel: Scheme of the celestial plane of the two interferometers, where NCP is the North Celestial Point, $d^2\Omega$ is the observed plane and δ is the distance to the source center. The images were created after Burke et al. (4)

one can easily unterstand, that we get the direction by

$$\vec{s} = \vec{s}_0 + \vec{\sigma}. \tag{2.2.5}$$

To improve our data collection, we increase now the numbers of elements in our interferometer. To simplify our equations we use the instrumental delay to cancel out the delay of the distance to the tracking center and can so equate the complex visibility.

$$V_{ij} = \int A(\vec{\sigma}) B_\nu(\vec{\sigma}) \exp(i2\pi b_{ij,\lambda}\vec{\sigma}) d\Omega, \tag{2.2.6}$$

where $S(v_0)$ is replaced with a radiating source element $B_\nu(\vec{\sigma})$ and i and j are the indices of the used baseline. If we express this in the natural given coordinate system by using a plane perpendicular to the tracking centre, which is commonly known as the (u, v) plane. If we transform Equation 2.2.6 we get

$$V_{ij}(\vec{s}_0, u, v) = \int A(l, m) B_\nu(l, m) \exp[i2\pi(ul + vm + wn)] d\Omega. \tag{2.2.7}$$

One can show in few steps, as shown by Burke and Graham-Smith (4), that we can easily substitute the integration over the angle with integrations over x and y, thus

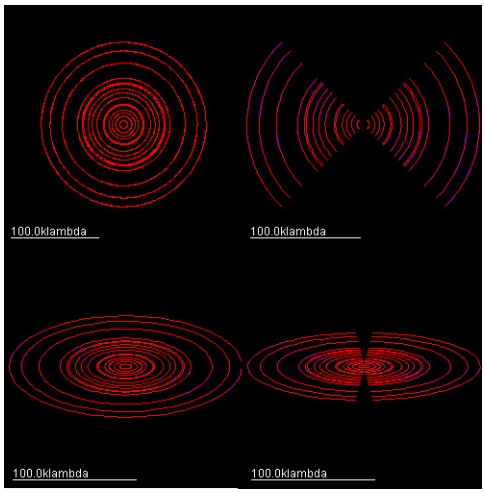

Figure 2.4: Effect of different parameters on the (u, v)-Plane, on the upper left the declination is 0° with an exposure time of 12h resulting in a circle, on the upper right the observing time is reduced resulting in a partial circle, on the lower left the declination was increased resulting in an elliptical shape, on the lower right the two parameters were both changed resulting in a partially elliptical shape. The image was created with the VLBI calculator of the Australian Telescope National Facility

resulting in

$$V(u,v) = A \int B(x,y) \exp[i2\pi(ux+vy)]dxdy. \tag{2.2.8}$$

For a VLBI interferometer it is often importan to get a good uv-coverage. This is mainly influenced by some parameters as shown in Fig.2.4 for the Australian Telescope Compact Array (ATCA). The first and obvious one is the setup of our telescopes, depending on the position and the distance between the telescopes. Adding more telescopes with different baselines leading to more data points which integrated over the time draw ellipses over the uv-plane. The observation time is the next important parameter. The longer the time the greater the angle of the ellipse. The last important parameter is the declination, which defines the ratio between the two major axis of the ellipse on the uv-plane.

2.2.2 TANAMI

The Data evaluated in this thesis is taken by the TANAMI program, the short form for Tracking Active galactic Nuclei with Austral Milliarcsecond Interferometry. Information on the TANAMI programm can be found in Kadler et al. (11). The TANAMI collaboration has its main goal to observe AGN at frequencies of 8.4GHz and 22.3GHz. At the initial start the program observed 43 sources and has quickly expanded to the state of

Table 2.3: Tabular with an overview of the TANAMI antennas.Listed are the name with the short form, the size of the dish and the location of the telescope. This table is adaptet from Müller (17)

Telescope	Diameter(meters)	Location
Parkes(PA)	64	Parkes, New South Wales, Australia
ATCA(AT)	5 × 22	Narrabri, New South Wales, Australia
Mopra(MO)	22	Coonabarabran, New South Wales, Australia
Hobart(HO)	26	Mt. Pleasant, Tasmania, Australia
Ceduna(CD)	30	Ceduna, South Australia, Australia
Hartebeesthoek(HA)[a]	26	Hartebeesthoek, South Africa
DSS43(DS)[b]	70	Tidbinbilla, ACT, Australia
DSS45[b]	34	Tidbinbilla, ACT, Australia
O'Higgins[c]	9	O'Higgins, Antarctica
TIGO(TI)[c]	6	Concepcion, Chile
Warkworth	12	Aukland, New Zealand
Katherine	12	Nothern Territory, Australia
Yarragadee(YG)	12	Western Australia
ASKAP	36 × 12	Murchinson, Western Australia

Note:

(a)Unavailable between Sept. 2008 and Sept. 2010
(b)Operated by the Deep Space Network of the National Aeronautics and Space Administration
(c)Operated by the German Bundesamt für Kartographie und Geodäsie (BKG)

more than 90 sources by 2015. Also it has the unique feature of being the only larger program taking data at declinations smaller than $-30°$ in the southern hemisphere. The scattering of the telescopes over Australia, Africa and Antarctic guarantees a good coverage with long baselines. The radio telescopes of the collaboration are along with the location and the size noted in Table 2.3 Since the campagne has a multiwavlength background it collaborates with data from several other telescopes of other spectral regimes. Since the sources of the TANAMI sample are taken from the Fermi/LAT programm, naturally there are data available. In the X-ray regime the collaboration with the Swift Telescope alongside the XMM-Newton Telescope makes an important amount of data available. Lastly, the close collaboration with the ANTARES group makes it possible to compare given data to detected neutrino events.

2.2.3 Analyzing VLBI Data

There are several steps to perform to analyze the VLBI data of the TANAMI programm. Normally it begins with precalibrating the data to the right phase and amplitude which is performed with the Astronomical Imaging Processing System (AIPS). This has to be done in order to get the information about the flux density. Since this was not part of the thesis no further information is given at this point, but can be aquired in Cotton (7) or Diamond (8). The second step is to create the clean images, which uses the algorithm of differential mapping. The program used to perform this step is DIFMAP and the information given is taken from Taylor (20) and from the internal help database of the program. To do this one first has to set up the most important parameters. The first one is the polarization, which is expressed through the stokes parameters and can basically be defined if we have circular or linear polarization. After that we bin the continuous data to discrete time intervals by averaging the signal over the interval. The third one is the weighting of the data. There are different approaches dependent on the scientific purpose of the image. Natural weighting weights the data points the same which is good for large resolutions, since the outer baselines have the same impact in the measurement as the short baselines. Uniform weighting is better for an increased sensitivity since the data is weighted with the visibility points, which are more numerous in the center due to the larger data coverage. The higher weighting on the inner baselines degrades the outer ones which decreases the resolution. In this thesis only uniformal weighting is used since the sensitivity is enough to resolve the core and a higher resolution improves the kinematic analyses. After this the data is reduced by flagging the data. This means we sort out the data which gives no contribution since the amplitude is close to zero. Also the data which varies too strongly during the observation is flagged. This is seen if the signal is stable over the measurement but shows some extreme error bars. After flagging the data we open the dirty map which is showing the Fourier transformed image. Our aim is to gain the reverse Fourier transformation by the differential mapping algorithm. The algorithm needs to be told where flux is expected and to tentatively place delta components which cleans the dirty image of the flux. When the flux is cleaned we have found a model which resembles our actual observation. The discrete delta components can be easily retransformed into our clean images. The cleaning process is shown in Fig. 2.5. After that we recalibrate the phases and amplitudes to regain the information about the flux densitys.

To get the plots out of the data from DIFMAP the tool which was used is the Interactive Spectral Interpretation System (ISIS).

With the finished clean files we have information about the jet structure, which we can use to calculate the velocity of the components. For this we set Gaussian components on the position of the peaks in the jet until the algorithm converges. The so found modell components show the position of the jet components and can then be used to calculate the velocity with a linear regression.

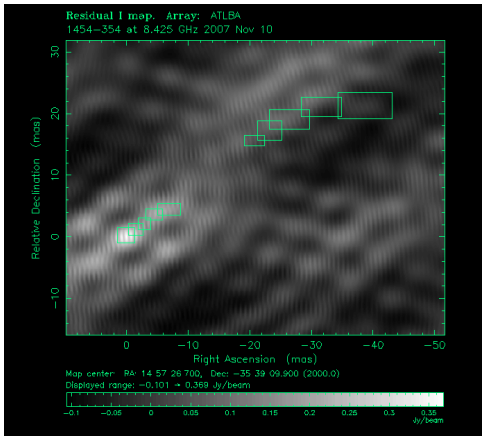

Figure 2.5: Example of the imaging process in Difmap, the green boxes define the area where the flux will be cleaned. In the image the flux has yet to be cleaned.

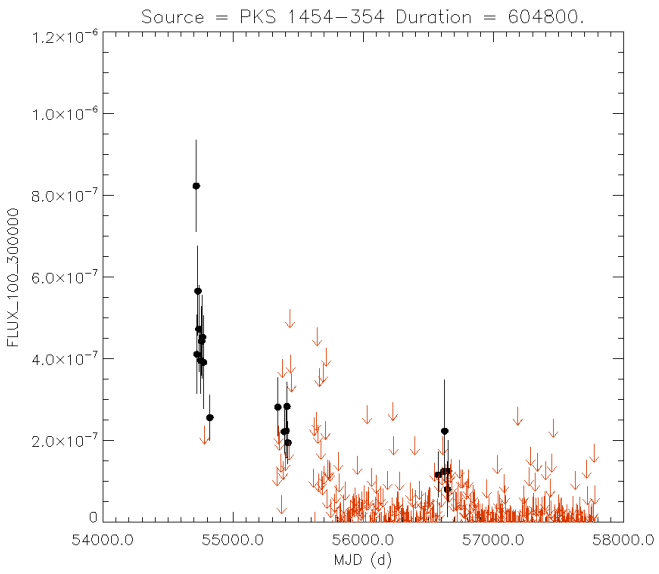

Figure 2.6: Fermi/LAT light curve over the last years where the y-axis shows the flux. The images are taken from the public Fermi/LAT data (Goddard Space Flight Center)

2.3 Previous Results

PKS 1454-354 is a FSRQ and was first discovered in the Molonglo Radio Telescope Survey. It is located at a redshift of $z = 1.424$. It showed a very high flux state on the 4th of September 2008 as is described in Abdo A.A. (1), where the information of this section can be found. This was observed in the Gamma-Band by the Fermi/LAT Satellite. On a timescale of hours the flux rose and decreased over the next two days to the normal level. This flaring state triggered some different follow up observations by Swift and the TANAMI programm. A TANAMI observation previous to the flare was also used in the analysis.

The Fermi satellite is equipped with the Large Area Telescope (LAT), which is a well suited instrument for surveying the sky due to the high field of view. It detects photons of the γ-ray regime with energies of 20 MeV to over 300 Gev. Through pair production of electrons and positrons the amount and energy of the incoming photons can be measured and thus evaluated. The photons were measured from 10° around the coordinates of the radio position and an unbinned likelihood was calculated to ensure that PKS 1454-354 contributes to the source of the γ-ray. The data was fitted with a power law and thus the flux could be estimated to $(1.29 \pm 0.15) \cdot 10^{-6} \frac{\text{ph}}{\text{cm}^2\text{s}}$ and showed a peak at $(1.7 \pm 0.4) \cdot \frac{\text{ph}}{\text{cm}^2\text{s}}$. The flaring maximum was between 03 and 06 UTC. The figures Fig. 2.6 and Fig. 2.7 show the measured Fermi fluxes of the last years with the high flare in 2008.

There are few observation instruments in the X-ray regime. Due to atmospheric limi-

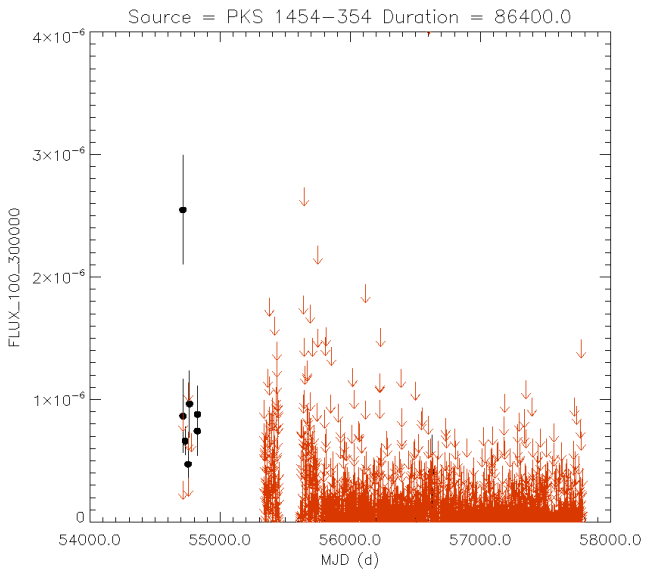

Figure 2.7: Fermi/LAT light curve over the last years but with a shorter binning than in fig.2.6 and thus showing more short term variability. The images are taken from the public Fermi/LAT data (Goddard Space Flight Center)

tations it is only possible to observe from space, where the limited size and the extremely low refractive coefficient makes instruments very expensive. For our purpose the best instrument is the SWIFT telescope since it is constructed for flaring follow-ups. SWIFT observed two different observations of the source, where the first one is from the 7th of September 2008 with an exposure time of 1.5 ks, and the second one from the 1st of January 2009 with an exposure of 9000 ks. This low exposure time results in a very small statistic and thus only an upper limit can be computed for the X-ray flux. The flux is therefore not higher than $6 \cdot 10^{-10} \frac{\text{erg}}{\text{cm}^2\text{s}}$ in the 20-100 keV regime.

Optical data was taken from the ATOM telescope in Namibia on the 6th and the 7th of September. The measured magnitudes for the two observations are $B = 17.01 \pm 0.02$ and $B = 16.83 \pm 0.02$. These can be transformed to flux density which can be used for the Spectral Energy Distribution (SED).

Lastly we have radio data of 13th September 2008 for 5 different frequencies. The values are 0.76 ± 0.08, 0.77 ± 0.02, 0.87 ± 0.02, 1.23 ± 0.07, 1.28 ± 0.08 at frequencies of 2.4, 4.8, 8.7, 18.5, 19.5 GHz. Comparing them with archive data shows that the radio flux has increased by 40% at that time. Figure2.8 shows an image of the radio regime from data of the 10th of November. Figure 2.9 shows the SED in the flaring state. The SED is important to calculate the spectral index of the source since the relation is given by $S_\nu \propto \nu^\alpha$. The value calculated from archival data yields $\alpha = 0.054$ if the data of the flare is used the photon index is computed to $\alpha = -0.10 \pm 0.01$.

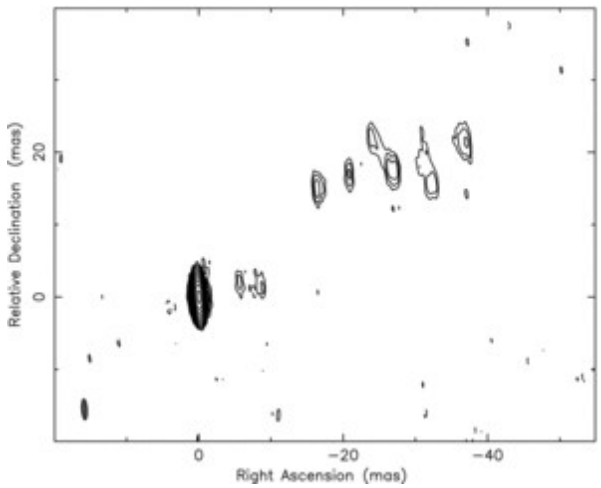

Figure 2.8: Image of the radio properties of PKS 1454-354 from the 10th November 2007 the image is taken from Abdo A.A. (1)

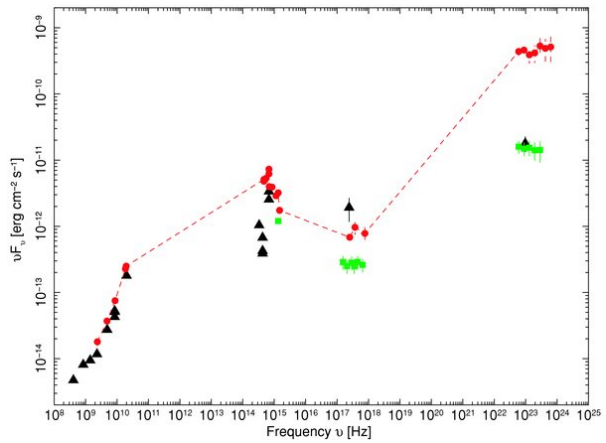

Figure 2.9: Plot of the spectral energy distribution of PKS 1454-354 during the flaring state. The plot is taken from Abdo A.A. (1)

3 Analysis of PKS 1454-354

3.1 Imaging of PKS 1454-354

The TANAMI antennas observed PKS 1454-354 at 7 different epochs from November 2007 until September 2012. For this data the clean files are shown in the Fig. 3.1 - Fig. 3.7. The images were then modelfitted to investigate the kinematic behavior of the jet components. Notable is the low resolution of Fig. 3.2 and Fig. 3.7. The resolution is highly dependant on the constellation of the telescopes, so when some large baselines are missing or scrapped due to low data reliability, the resolution suffers. The resolution which is here defined through the size of the beam (which is comparable to the point spread functions in other areas of imaging physics) is shown in Table 3.1 along with the constellation of the telescopes. The total flux density S_{tot} is gained through integration of the flux density over the map. S_{peak} is the highest measured flux in the area of a beam. The noise ratio σrms is calculated by measuring the flux in an empty area. The position angle is the angle between the orientation of the core component and the beam orientation, or to put it more simply the angle between the major axis of the core and the beam. Another dependance of the beam is shown in Section 2.2.1 with the declination of the source, which changes form with different (u, v) coverages and thus with different epochs.

As mentioned in the section above, an important part of correlating our jet model with Gaussian components is the step of modelfitting and thus getting the movement of the jet components. Since we are combining a theoretical model with our experimental observed data we have to check the reliability of the components. This can be done as shown in Kovalev et al. (14) through calculating the theoretical resolution of the virtual telescope and comparing it to the modelfit components. The equation used for this is given by

$$\Theta_{\mathrm{lim}} = b_{\psi} \cdot \sqrt{\frac{4 \ln 2}{\pi} \ln\left(\frac{\mathrm{SNR}}{\mathrm{SNR} - 1}\right)}, \tag{3.1.1}$$

with b_{ψ} as the beam size, which is approximated as a circle with the major axis as radius, and the SNR of the component, defined through $\mathrm{SNR} = \frac{S_{\mathrm{comp}}}{\sigma_{\mathrm{comp}}}$. If the theoretical components do not match the realistic resolution the major axis is set to the theoretical resolution of the telescope. The results of the modelcomponents are shown in Table 3.2.

Table 3.1: Table of the basic paramteters of the 7 imaged epochs, where are shown the date of the observation, the constallation of the telescope at the measurement, the total flux density S_{to}, the peak flux per beam S_{peak}, the noise of the backgroung σ_{rms}, the major and minor axis of the beam b_{maj}/b_{min} and the position angle(P.A.).

Date YYYY-MM-DD	Array Configuration	S_{tot} [Jy]	S_{peak} [Jy/beam]	σ_{rms} [mJy/beam]	b_{maj} [mas]	b_{min} [mas]	P.A. [°]
2007-11-10	PKS-AT-MP-HO-CD-HA	0.418	0.341	0.11	1.31	0.31	3.46
2008-06-09	AT-PA-MO-HO-CD-HA	0.549	0.576	0.19	1.53	1.13	82.3
2008-11-27	AT-PA-MO-HO-CD-OH-TC-DS	0.567	0.419	0.41	0.64	0.32	61.7
2009-09-05	CD-HO-MO-PA-TC-TI	0.829	0.551	0.33	1.62	0.29	9.7
2010-05-07	AT-CD-HO-MP-PA-TC-TI	0.530	0.599	0.23	1.44	0.43	27.5
2011-08-13	AT-CD-HO-KE-PA	0.711	0.469	0.58	1.18	0.48	9.8
2012-09-15	AT-CD-HO-KE-PA-HA-MP-TC-YG	0.653	0.791	0.28	1.94	1.05	16.2

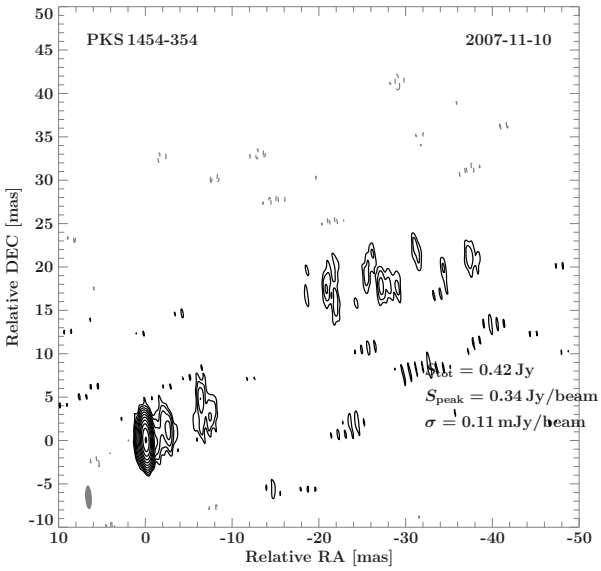

Figure 3.1: Clean image of the Epoch A taken on 10th of November 2007, in the image the total flux S_{tot}, the measured peak flux S_{peak} and the noise ratio σ_{rms} are noted.

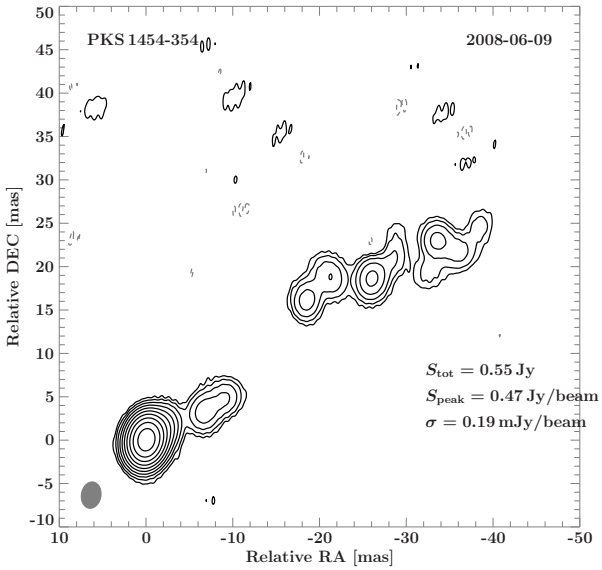

Figure 3.2: Clean image of the Epoch A taken on 9th of June 2008, in the image the total flux S_{tot}, the measured peak flux S_{peak} and the noise ratio σ_{rms} are noted.

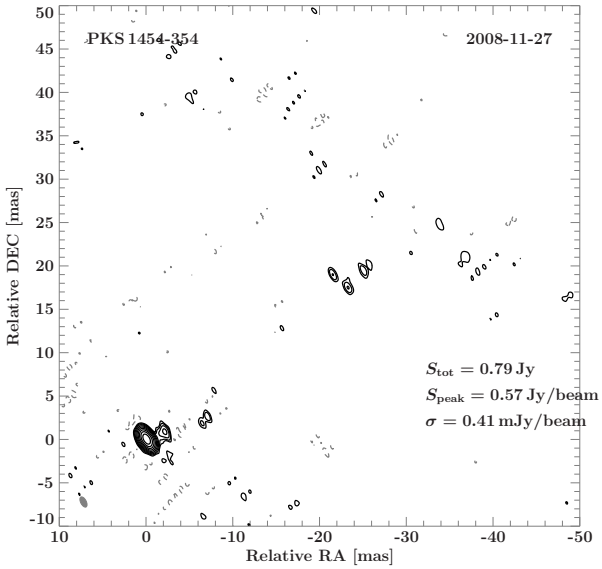

Figure 3.3: Clean image of the Epoch A taken on 27th of November 2008, in the image the total flux S_{tot}, the measured peak flux S_{peak} and the noise ratio σ_{rms} are noted.

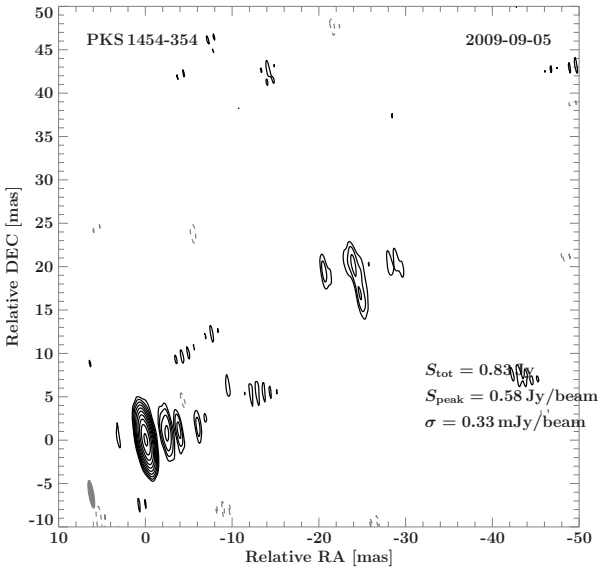

Figure 3.4: Clean image of the Epoch A taken on 5th of September 2009, in the image the total flux S_{tot}, the measured peak flux S_{peak} and the noise ratio σ_{rms} are noted.

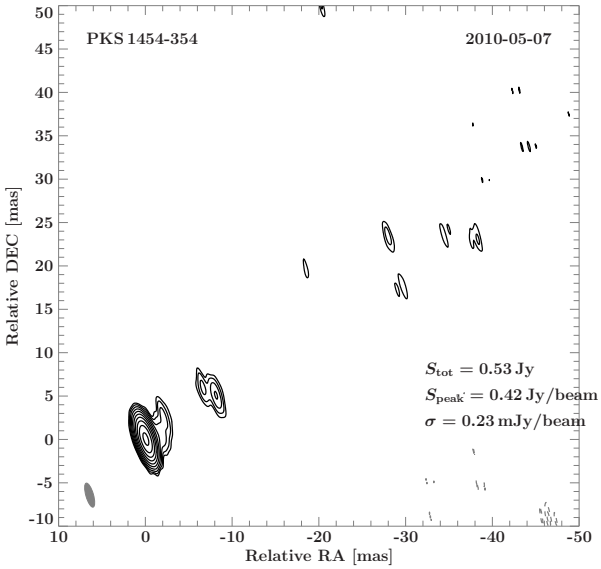

Figure 3.5: Clean image of the Epoch A taken on 7th of May 2010, in the image the total flux S_{tot}, the measured peak flux S_{peak} and the noise ratio σ_{rms} are noted.

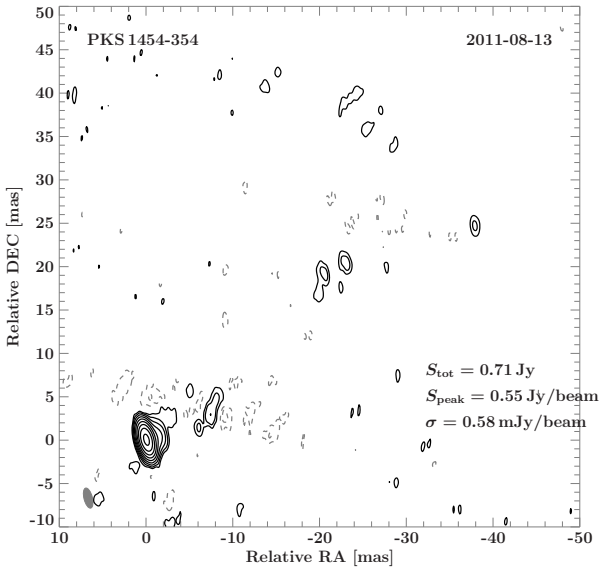

Figure 3.6: Clean image of the Epoch A taken on 13th of August 2011, in the image the total flux S_{tot}, the measured peak flux S_{peak} and the noise ratio σ_{rms} are noted.

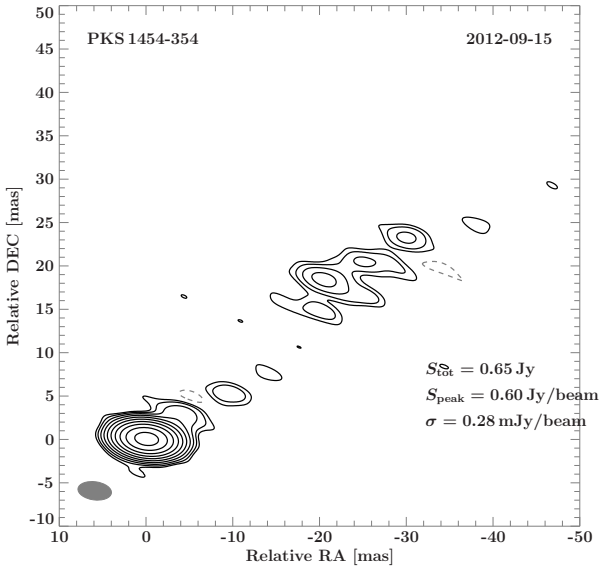

Figure 3.7: Clean image of the Epoch A taken on 15th of September 2012, in the image the total flux S_{tot}, the measured peak flux S_{peak} and the noise ratio σ_{rms} are noted.

Table 3.2: Table of the modelfitted components, where S is the flux density of the fitted component, R and Θ are polar coordinates, a_{maj} and a_{min} are the axis of the fitted components, with a_{min} only listed for the core components, since the other components are circular. The position angle (P.A.) is the angle between the beam and the majoraxis, the ID is the identity number of the component and Θ_{lim} is the theoretical resolution.

S [mJy]	R [mas]	Θ [deg]	a_{maj} [mas]	a_{min} [mas]	P.A. [deg]	ID	Θ_{lim} [mas]
390.95		11.09	0,318	0.265	39.3	Core	0.020
8.98	2.54	-55.75	3,071		32.5	1	0.134
1.66	7.84	-64.51	0.000		28.6	2	0.317
10.78	28.36	-50.84	7.299		45.00	0	0.122
492.78	0.01	113.60	0.718	0.000	-16.65	Core	0.038
12.86	8.70	-60.65	0.649		69.44	2	0.239
11.74	23.38	-48.46	0.925		60.95	0	0.250
8.95	32.46	-52.88	0.000		73.30	0	0.288
10.15	37.13	-55.83	1.154		56.31	0	0.270
742.99	0.00	148.97	0.464	0.390	17.63	Core	0.035
26.73	1.76	-82.54	3.455		23.96	1	0.186
10.26	28.87	-50.92	1.927		45.00	0	0.301
786.20	0.01	-174.48	0.595	0.423	-1.99	Core	0.022
18.63	3.05	-88.15	2.990		74.05	1	0.144
21.07	30.81	-58.84	7.329		23.20	0	0.135
498.21	0.04	-158.25	0.477	0.203	-79.03	Core	0.017
14.15	2.18	-78.74	0.000		27.90	1	0.104
9.53	8.30	-42.74	0.156		33.69	2	0.127
1.90	42.13	-57.64	0.000		41.42	0	0.299
584.27	0.03	108.59	0.225	0.000	-75.57	Core	0.036
55.33	1.12	-77.61	0.821		21.99	1	0.117
34.12	6.52	-64.31	7.331		21.50	2	0.149
18.03	26.53	-46.43	5.326		90.00	0	0.206
11.93	32.24	-50.91	0.001		45.00	0	0.254
614.36	0.01	43.46	0.650	0.236	-74.02	Core	0.026
14.08	3.97	-68.20	2.246		39.81	1	0.171
4.19	23.28	-47.41	1.383		34.38	0	0.317
6.20	27.35	-48.92	0.344		66.04	0	0.260

Component	$v_{app,vec}$	$\beta_{app,vec}$	$v_{app,dist}$	$\beta_{app,dist}$
C1	-0.76 ± 0.63	-51 ± 42	-0.79 ± 0.59	-53 ± 40
C2	0.19 ± 0.14	12.6 ± 9.3	-1.33 ± 0.11	-89 ± 7.6

Table 3.3: Calculated velocities for the two components

3.2 Kinematic of the jet components

The reason why we put the high effort of finding a theoretical model for our experimental data is to calculate the most exact velocity and to describe the jet kinematic. This can be used for most of the information we can draw about AGN and to improve the unterstanding of these objects. To compute the velocity we need to identify the components through the different epochs. This is quite the tricky part since there are many possible solutions and we have to evaluate the right one which leads to a lot of discussion. The velocity itself can then be found easily via linear regresion since the velocity of the jet components should be constant across the observed time scales. As already described in Section 2.1.5 the jet components are often moving with velocitys higher than the speed of light due to projection effects. As also described in this section we can use the velocitys of the components to get the apparent angle using Equation 2.1.13. The angle to the LOS can be calculated through the jet to counter-jet ratio. If there is no counter-jet visible, like in our case, the least we can do is to compute an upper limit whith the sensitivity of the telescope. This can easily be justified: if the counter-jet would exceed the sensitivity of the telescope we would see it in the image. Since this is not the case it can not be higher than the sensitvity and is therefore below our limit. The time evolution of the jet components over the epochs is shown in Fig. 3.8. The calculated velocities and Lorentz factors of the identified components are shown in Table 3.3

3.3 Variability of the flux density

As we showed in the previous section, the flares had different intensities in their respective regimes. Also the maximum of the flares is located at different times. Due to the lack of data the maximum of the radio peak could not be located in the paper of Abdo A.A. (1). With the addition of further epochs we can pinpoint the maximum of the radio flare and also draw more conclusions about the increase. The flux density values were already shown in Table 3.1. We can use them to plot them against the time which is shown in Fig. 3.10. We can see that the flux maximum is between the third and the fourth epoch. The highest flux density value which was measured is (0.829 ± 0.124)Jy. The error in the flux density is estimated to be 15% of the measured flux density. This estimation is according to Böck (5).

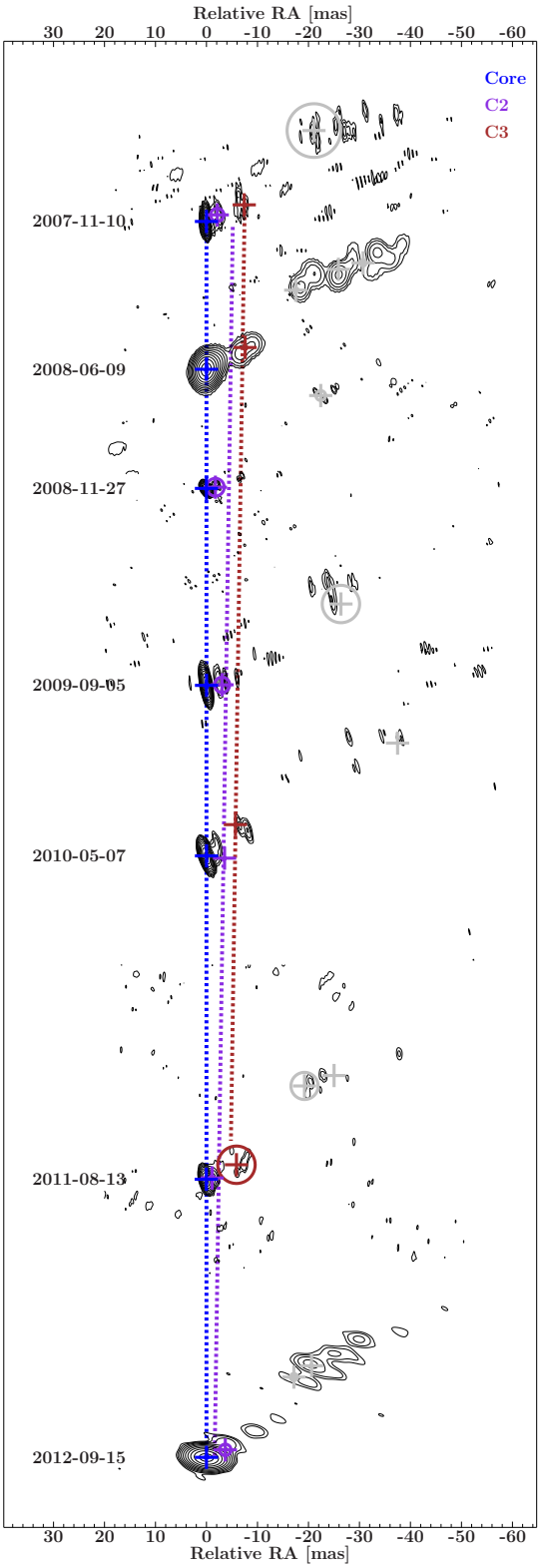

Figure 3.8: Plot of the seven epochs placed under each other with matching distances. This shows the kinematic of the inner two components.

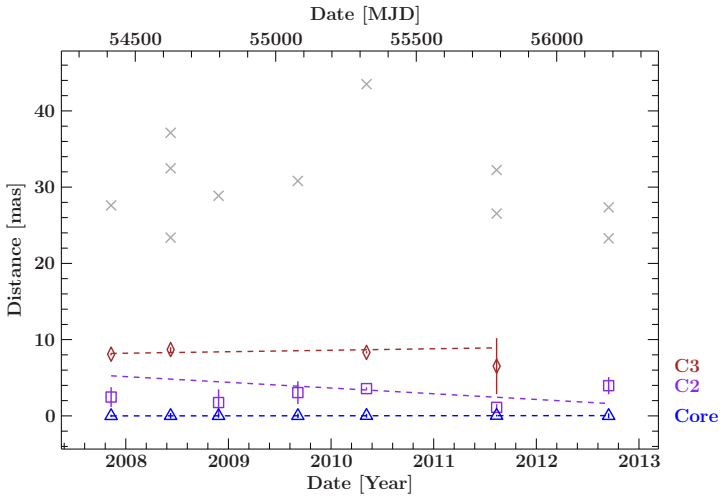

Figure 3.9: In this plot the distance is plotted against the time. The main difference to the time evolution plot above is that the distance is not taking the vectorial velocity in account

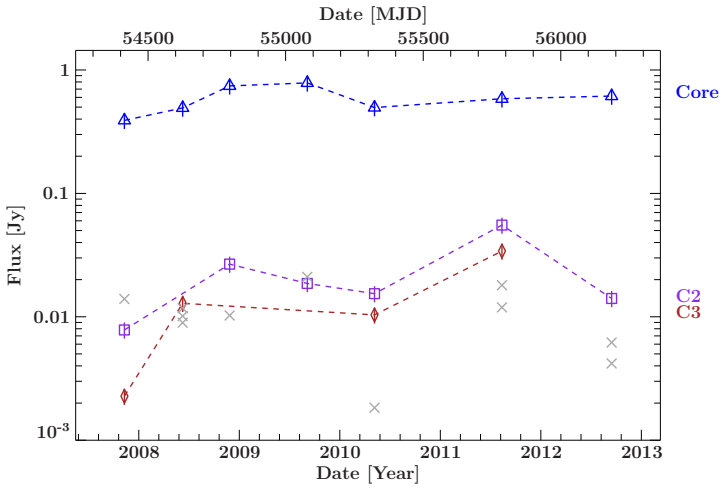

Figure 3.10: Change of the Flux over the different epochs, notable is the increasing at first with the maximum between the third and the fourth epoch. The error of the flux is estimated to 15% according to Böck (5)

4 Discussion on PKS 1454-354

A difficult part of the jet kinematic analysis is to identify the components over the different time epochs. This is even more complicated due to the fact that the components are not visible in every epoch. In Fig. 3.9 the distance of the component is plotted against the time epoch, in Fig. 3.8 the plot takes the directions in account. A good indicator for a valid identification is if the components lie on a straight line because AGN jet features are known to travel in first order on ballistic tracks (as found in Lister et al. (15)). There were two possible connections of the inner components. The first possibility alligns the inner components with a strong outwards moving dynamic. Extrapolating this line to the core leads to an intercept at July 2008 which is quite close to the flare. If we calculate the velocity for this possibility the velocity is roughly around 100 c, which is very unlikely. Therefore this scenario wes rejected and replaced through the second possibility, which links the inner components with slower movements. There were components in the first and fifth epoch, where the major axis diverged to a very small point component below the resolution of the telescope array. Equation 3.1.1 yields the value of the theoretical possible resolution of our telescope. We can use it therefore to calculate the theoretical resolution and determine a limit for the major axis of the component. In Section 2.1.4 we showed the dependancy on the brightness temperature to the major axis. Since we manually modified the size of our component, the brightness temperature has therefore to be neglected. The theoretical resolution of the telescope is calculated in Table 3.2.
We can use Equation 2.1.16, to rearrange it for yielding φ. This leads to

$$\varphi = \arccos\left[\frac{1}{\beta}\frac{\left(\frac{S_{\text{jet}}}{S_{\text{counterjet}}}\right)^{\frac{1}{3-\alpha}} - 1}{\left(\frac{S_{\text{jet}}}{S_{\text{counterjet}}}\right)^{\frac{1}{3-\alpha}} + 1}\right], \tag{4.0.1}$$

where $\beta = \frac{v}{c}$, the quotient $\frac{S_{\text{jet}}}{S_{\text{counterjet}}}$ describes the jet to counterjet ratio and α the spectral index. We can calculate a lower limit for φ by setting $\beta = 1$. The spectral index is as we saw in Section 2.3 at $\alpha = 0.010$ during the flare and in the normal state at $\alpha = 0.054$. Since the spectral index has a very small impact on the result here, we are going to approximate it with $\alpha = 0$ to simplify the equation. PKS 1454-354 shows no significant counterjet which leads to the problem of calculating the jet to counterjet ratio. Since we are approximating a limit for the angle we can estimate the jet to counterjet ratio by setting the flux density of the counterjet to our noise level of the best epoch.

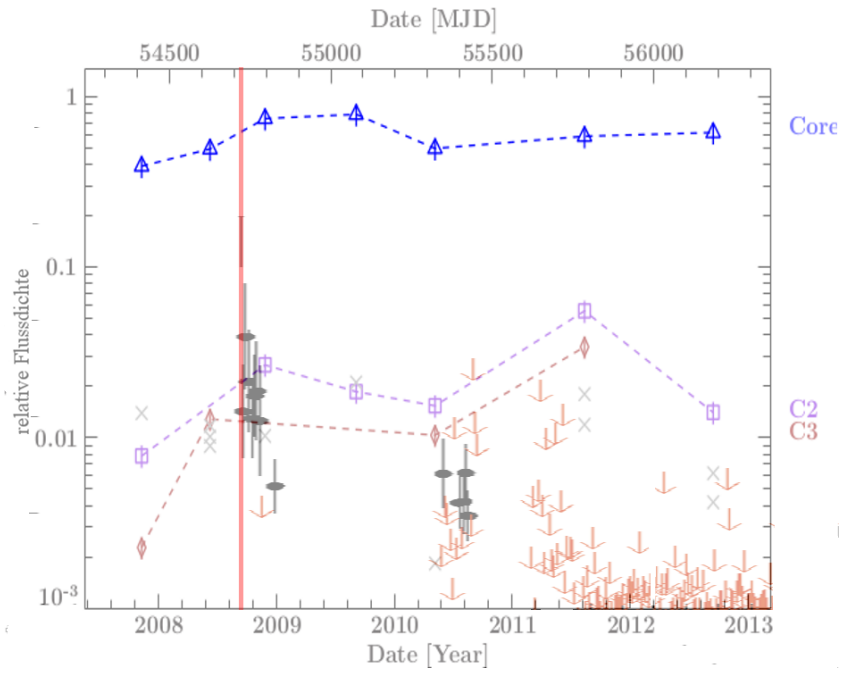

Figure 4.1: Plot of the relative flux increase in the source after the flare, the flux density of the core in the radio regime is shown in the upper part, for the γ-regime in the lower part. The image was created through overlapping the Fermi/LAT lightcurve with the measured radio data of the TANAMI sample. The red marking indicates the γ-ray flare which propagates to lower frequencies

Inserting it into the equation yields for the limit of $\varphi < 44°$.

The theoretical models proclaim that flares in an AGN are produced by an adiabatic shock-in jet model, as it is shown in the paper of Marscher et al. (16). The jet is moving outward at highly relativistic speeds and collides with a slower phase causing a shock wave in the jet. This produces synchrotron radiation at very high energys which are quickly decaying to lower energies. This can be seen in the radio regime by a new emerging component which is induced in the jet. Our data shows no signs of a new emerging component, which is possibly due to the low resolution of our telescope. Since we study a FSRQ we might have a very small inclination angle to the LOS and the newly emerging component is moving with a slow apparent velocity. This might lead to overlapping with the core component which can explain the measured increase in flux density in the radio regime. In Fig.4.1 the Fermi/LAT Lightcurve is time overlapped with the measured radio flux density, where the red marking is indicating the flare. With proceeding time the γ- ray emmision of the source is propagating to lower frequencies until it reaches the radio band in 2009 where the radio emmision in our measured wavelength reaches its maximum around 0.829 ± 0.124 Jy. This is consistent with the value in the paper of Abdo A.A. (1) where the flux is measured to 0.87 ± 0.02 Jy.

5 Conclusion and Outlook

In the thesis seven epochs of the Flat Spectrum Radio Quasar PKS 1454-354 were observed at 8.4 GHz. They were imaged with the program Difmap and after that modelfitted to calculate the jet kinematic.
The apparent vectorial velocities could be computed to $v_1 = -(0.76 \pm 0.63)$mas/year and $v_2 = (0.19 \pm 0.14)$mas/year. The velocities can be transformed in multiples of the speed of light, and hence $\beta_{app,1} = -(51 \pm 42)$ and 4.8 ± 6.8. The angle to the line of sight could be estimated using the jet to counterjet ratio. The cflux density of the counterjet was approximated with the noise level of the observation, resulting in an upper limit of $\varphi < 44°$.
The maximum of the radio flare could be constrained to the third quarter of 2009 with a flux density value of (0.829 ± 0.124)Jy, which is consistent with the paper of Abdo A.A. (1).
Further Analyse can provide a lower limit for the velocity of the jet using the limit for φ. To improve the fit of the modelcomponents more observation data is useful. Since the inner components are not visible in all epochs more epochs could help to find a better fit and reducing the error on the measured kinematic. This could also give the possibility to make assumptions on the currently diffuse outer components of the jet. Also the observation in other radio wavelengths could give further insights on the current jet kinematic.

Bibliography

[1] Abdo A.A.,& Fermi Collaboration, 2009,ApJ 697

[2] Antonucci R., 1993, ARA&A 31, 473

[3] Beckmann V., Shrader C., 2012, Active Galactic Nuclei, Wiley VCH

[4] Burke B. F., Graham - Smith F., 2010, An Introduction to Radio Astronomy, Cambridge University Press

[5] Böck M., 2012, PhD thesis, Naturwissenschaftliche Fakultät, Friedrich-Alexander-Universität Erlangen-Nürnberg

[6] Carroll B. W., Ostlie D. A., 2014, An Introduction to Modern Astrophysics, Second Edition, Pearson Education Limited

[7] Cotton W. D., 1995, Very Long Baseline Interferometry and the VLBA, Ed. by Zensus J. A., Diamond P. J. and Napier P. J., Vol. 82, Astronomical Society of the Pacific Conference Series

[8] Diamod P. J., 1995, Very Long Baseline Interferometry and the VLBA, Ed. by Zensus J. A., Diamond P. J. and Napier P. J., Vol. 82, Astronomical Society of the Pacific Conference Series

[Fermi] Public Fermi Data, National Aeronautics and Space Administration, Goddard Space Flight Center

[10] Kadler M., 2015, Extragalactic jets, Lecture on extragalactic jets held in the summer term

[11] Kadler M., Ojha R., & TANAMI Collaboration, 2015, AN 336, 499

[12] Kellermann K. I., Sramek R., Schmidt M., et al., 1989, AJ 98, 1195

[13] Kembhavi A. K., Narlika J. V., 1999, Quasars and Active Galactic Nuclei An Introduction, Cambridge University Press

[14] Kovalev Y. Y., Kellermann K. I., Lister M. L., et al., 2005, ApJ 130, 2473

[15] Lister M., Cohen M.H., et al., 2009, AJ 138

[16] Marscher A. P.,Gear W. K., 1985, ApJ 298

[17] Müller C., 2014, PhD thesis, Institut für Physik und Astronomie, Julius-Maximilians-Universität Würzburg

[18] Ojha R., Kadler M., Böck M., et al., 2010, A&A 519, 45

[19] Rybicki G. B., Lightman A. P., 1979, Radiativ Processes in Astrophysics, New York: Wiley

[20] Taylor G., 1997, The DIFMAP Cookbook

[21] Urry C.M., Padovani P., 1995, PASP 107, 803

[VLBI Calculator] VLBI Calculator, Australian Telescope National Facility

Danksagung

Ich danke allen die zu dem Erfolg dieser Arbeit beigetragen haben. Dies sind vor allem Prof. Dr. Matthias Kadler der mich durch den Erstellungsprozess der Arbeit begleitet hat und der mir viel durch Diskussion und hilfreichem Feedback geholfen hat, die Qualität der Arbeit zu steigern. Desweiteren möchte ich mich bei Prof. Dr. Karl Mannheim bedanken, der durch seine Leitung am Lehrstuhl für Astronomie den Rahmen für diese Arbeit geliefert hat.
Ich möchte mich bei meinen Kommilitonen Florian Rösch, Amar Hekalo und Michael Kreter bedanken, die mein Werk Korrektur gelesen und so geholfen haben die vielen kleinen Fehlerteufel in der Thesis zu minimieren.
Ein weiterer Dank gilt an dieser Stelle allen Anhängern des Lehrstuhls für Astrophysik und der AG Kadler, die mit vielen Diskussionen und offenen Ohren immer eine Anlaufstelle waren um mein Verständis zu erweitern. Dabei findet auch unser Bacheloranden Büro, bestehend aus Michael Blank, Manuel Dörr, Lukas Schrenk, Johannes Kammerer, Florian Rösch und Amar Hekalo, besondere Erwähnung die für eine angenehme Atmosphäre gesorgt haben, in der es sich entspannt hat arbeiten lassen.
Zum Abschluss möchte ich meinen Eltern bedanken die mich immer im Studium unterstützt haben und dabei eine große moralische Stütze waren.

Selbstständigkeitserklärung

Ich versichere, die vorliegende Arbeit selbstständig nach allgemeiner Studien- und Prüfungsordnung für die Bachelor- und Masterstudiengänge (ASPO) an der Julius-Maximilians-Universität Würzburg verfasst und keine anderen als die angegebenen Quellen und Hilfsmittel benutzt, sowie keiner anderen Prüfungsbehörde zur Erlangung eines akademischen Grades vorgelegt zu haben.

Würzburg, den 15. Februar 2017

Stefan Lindeholz